# Biostructural Science Inspired by Next-Generation X-Ray Sources

Sol M. Gruner[1,2,3] and Eaton E. Lattman[4,5,6]

[1]Department of Physics, [2]Cornell High Energy Synchrotron Source (CHESS), [3]Kavli Institute at Cornell for Nanoscale Science, Cornell University, Ithaca, New York 14853; email: smg26@cornell.edu

[4]Hauptman-Woodward Medical Research Institute, Buffalo, New York 14203

[5]Department of Structural Biology, School of Medicine and Biomedical Sciences, SUNY Buffalo, Buffalo, New York 14203

[6]BioXFEL Center, Buffalo, New York 14203

Annu. Rev. Biophys. 2015. 44:33–51

First published online as a Review in Advance on February 26, 2015

The *Annual Review of Biophysics* is online at biophys.annualreviews.org

This article's doi: 10.1146/annurev-biophys-060414-033813



## Keywords

microcrystallography, nanocrystallography, biomolecular solution scattering, synchrotron radiation sources, X-ray free-electron laser, energy recovery linac, bright storage ring sources

## Abstract

Next-generation synchrotron radiation sources, such as X-ray free-electron lasers, energy recovery linacs, and ultra-low-emittance storage rings, are catalyzing novel methods of biomolecular microcrystallography and solution scattering. These methods are described and future trends are predicted. Importantly, there is a growing realization that serial microcrystallography and certain cutting-edge solution scattering experiments can be performed at existing storage ring sources by utilizing new technology. In this sense, next-generation sources are serving two distinct functions, namely, provision of new capabilities that require the newer sources and inspiration of new methods that can be performed at existing sources.

## Contents



## INTRODUCTION

Synchrotron radiation (SR) methods have vastly expanded the ability to determine the molecular structure and properties of biological materials. This accomplishment is a direct consequence of the steady improvements in storage-ring-based SR facilities that have enabled diffraction experiments not feasible with conventional X-ray machines. Recently, next-generation synchrotron X-ray sources with greatly enhanced capabilities, e.g., X-ray free-electron lasers (XFELs) (64), energy recovery linacs (ERLs) (14), and ultra-low-emittance storage rings (UESRs) (13), have moved from concept to feasible implementation.

XFELs, the first of the next-generation sources (NGS) to come online, have already catalyzed novel experimental approaches in biostructural science, which have been excellently reviewed elsewhere (11, 30, 100). Our intent with this review is somewhat different from that of prior reviews and is based on two observations. First, routine availability of NGS is still the better part of a decade away; therefore, most experiments over the coming decade will continue to be performed at existing storage ring sources. Second, novel experimental approaches inspired by NGS experiments are being developed at existing storage ring sources.

To make these observations concrete, consider a proof-of-principle serial microcrystallography experiment (17) demonstrated at the Linac Coherent Light Source (LCLS) at SLAC (now SLAC National Accelerator Laboratory), the world's first hard XFEL. What, specifically, is novel about this experiment? Novelty is not confined to the XFEL source: The X-ray beamline, the sample delivery system, the X-ray detector, the data collection protocol, and the way in which the data were handled and analyzed are quite different from what is found at conventional crystallographic beamlines. This begs a question: If one were to likewise reconsider all parts of the crystallographic experiment in terms of in-principle physical limits, could one perform significantly more advanced serial microcrystallography at storage ring sources? The answer, as we shall show, is almost certainly yes.

This review is, therefore, forward-looking and focused on experiments that are likely to evolve over the next decade at existing storage ring sources, as well as at NGS. We identify specific future methods that are suggested by recent advances in order to provide a roadmap for future research. In some cases this involves the development of technology initiated at storage rings that will come to fruition at NGS. In other cases fruition will arrive at existing storage ring sources, such that the primary role of NGS will be inspiration and motivation.

## SERIAL MICROCRYSTALLOGRAPHY

Serial microcrystallography (SMX) refers to techniques that obtain atomic structure from multiple microcrystals. The use of multiple crystals to obtain structure dates back to the very beginnings of protein crystallography, but the ability do this with microcrystals is very much at the cutting edge of biostructural research. The scientific motivation is the assumption that many important protein systems that are difficult to obtain as large single crystals may be more readily available as many small, high-diffraction-quality crystals (34, 46, 68, 79, 102). For the purposes of this review, microcrystallography refers to crystals that are less than a few microns across; the distinguishing feature is that the crystals are too small to allow complete data sets to be obtained from a single crystal before radiation damage becomes limiting. Therefore, our use of the term microcrystallography includes nanocrystallography.

Successful demonstration of SMX experiments has driven much of the excitement at XFELs (11, 20, 48, 49, 60, 104). Significantly, examination of a seminal SMX XFEL experiment (17) reveals that almost every aspect of the experiment differs from routine crystallography at storage rings, leading to an important question: What are the limits in principle of what can be done at other bright sources, including present and future storage rings and ERLs, if one reconsiders the entire crystallography experiment? For example, will SMX be routinely performed at non-XFEL sources? This answer is important because the availability of XFEL beamlines will be limited for at least the better part of the next decade.

### What Is Required for a Complete Data Set?

Proof-of-principle XFEL experiments involved crystals that were typically a few microns in size, so consider the number of crystals that is needed to obtain a complete data set if each crystal has a volume of, say, $(2\ \mu m)^3$. Further, assume a unit cell size on the order of 100 Å across. Sliz et al. (94) based their examination of this issue on the experience at the time, i.e., using cryocooled crystals, phosphor-coupled CCD (charge-coupled device) detectors, and typical state-of-the art macromolecular beamlines at storage rings in 2003. They concluded that complete data sets at 3.5 Å resolution required crystals roughly $(20\ \mu m)^3$. Because radiation damage for cryocooled crystals scales linearly with dose (42), i.e., with energy absorbed per unit mass, data collection is ultimately limited by the total number of protein molecules involved. A crystal of $(20\ \mu m)^3$ has the same number of proteins as $10^3$ cryocooled crystals, each with a volume of $(2\ \mu m)^3$. For the sake of reference, call this a worst-case scenario because the Sliz et al. (94) scenario was based on extrapolations from experience and was not an optimization based on first principles. One fully expects that elimination of background scatter from beamline optics or reduction of detector noise would reduce the required number of crystals.

Holton & Frankel (43) started from first principles and assumed nearly ideal photon background and photon detection. They found that a complete data set with a signal-to-noise ratio of 2 at 2 Å resolution would be attainable from a cryocooled perfect lysozyme crystal sphere 1.2 μm in diameter. They noted that this diameter is further reduced by roughly a factor of 2 to 3 if photoelectron escape effects (67, 84) are taken into account; the resultant estimate is a reduction in volume by a factor of approximately 10. Lysozyme has roughly one-tenth the unit cell volume considered in the previous paragraph ($10^6$ Å$^3$), but the resolution considered is higher (2 Å versus 3.5 Å). It is reasonable, therefore, to say that in a best-case scenario (further discussed below) one cryocooled crystal 2 μm across should yield a complete data set at ~2 Å resolution for a unit cell approximately 100 Å across. Thus, the best- and worst-case scenarios as described above bracket

the number of 2-μm crystals required for complete 2 Å data sets to be from 1 to $10^3$ cryocooled crystals. This finding is supported by recent results at PETRA III (34).

How many ~10-keV incident X-rays will cause severe radiation damage to the 2-μm crystal? Although this number is dependent on the desired resolution and varies from one type of protein to another, a rule of thumb is that a 20-MGy dose limits the diffraction resolution to 2 Å (42, 45). A layer of protein or water 2 μm thick absorbs approximately $10^{-3}$ of the incident X-rays. Assume a beamline capable of delivering $10^{12}$ X-rays into the $(2\text{-}\mu m)^2$ cross-sectional area of the crystal. Some beamlines already exceed this (72), and brighter sources under development will increase this by orders of magnitude (14). This corresponds to $10^9$ absorbed X-rays in the $(2\ \mu m)^3$ volume, which is a dose rate of 200 MGy/s. The crystal will last ~0.1 s, which is the best-case-scenario time for a complete data set. For the worst case, assume the crystals are delivered serially into the beam one after the other; then the time to get a complete data set from 1,000 crystals is 100 s.

The above estimates are for cryocooled crystals. How about noncryocooled crystals? In round numbers, cryoprotection increases the number of absorbed X-rays to a given level of radiation damage by a factor of 100 if delivered quickly (66), so the best- and worst-case scenarios given above scale to $10^2$ and $10^5$ noncryocooled crystals, respectively, with corresponding total exposure times of 10 s and $10^4$ s. These numbers of crystals sound big, but the total volume of protein involved is actually modest: A single conventional crystal 200 μm on a side has the same volume as $10^6$ of the 2-μm crystals.

Even if the worst case takes ten times longer, the data collection times are still on the order of a day for a complete data set. And with forthcoming synchrotron sources with orders of magnitude more brightness, the time estimates fall by corresponding orders of magnitude. The important conclusion is that serial microcrystallography is feasible in principle at many types of existing synchrotron sources, and even more so with forthcoming brighter sources. Very recent first (and, therefore, not ideally optimized) results at PETRA III support this conclusion (98).

Obviously, the above estimates do not take into account many practical problems of implementation, such as crystal manipulation, heating, or orientation. But these problems are ones of engineering, not fundamental diffraction physics. With enough clever engineering effort, most practical problems can be resolved. This is precisely the philosophy that was and is being successfully taken in the case of microcrystallography at the XFELs, hence the title of this review.

## Experimental Considerations for Serial Microcrystallography

In the following sections we examine the literature on approaches to practical implementations and extrapolate areas in need of attention.

**Beam brightness.** Practical SMX is dependent upon the ability to focus sufficient and suitable X-ray flux onto a microcrystal to determine a structure in a reasonable amount of time. In this regard, what beam characteristics are important?

X-ray beams are characterized by their spectral brightness (X-rays/s/$mm^2$/$mrad^2$/0.1% bandwidth). The units indicate that X-ray beams, being electromagnetic radiation, are subject to the brightness theorem, a formulation of Liouville's theorem (12, 54). In practice, this means that the spectral brightness is at best constant along the beam path and that one may trade beam width for divergence, as long as the product of the two is kept constant. Both spectral brightness and transverse coherence are inversely proportional to the transverse electron emittances, defined as proportional to the product of the generating electron beam width and divergence transverse to the direction of electron beam propagation. This is the primary motivation behind the quest for

ever-brighter synchrotron sources: the smaller the electron beam emittances, the brighter the potential X-ray beams, which translates in turn to potential to put more X-rays into a low-divergence microbeam. Note the word "potential." Although a given electron emittance sets an upper bound on the X-ray beam spectral brightness and coherence, there are always ways to lose X-rays and lower the brightness (14, 33).

Just as with visible light, the diffraction limit set by the wavelength, $\lambda$, of the radiation determines the ultimate smallest width, $\Delta x$, and angular divergence, $\Delta\theta$, as $\Delta x \Delta\theta \geq \lambda/4\pi \approx 8$pm for 10-keV X-rays. The emittance of PETRA III, among the world's brightest rings as of 2014, is ~1 nm, about 100 times the diffraction limit. UESRs, and especially ERLs on the drawing boards, would approach the diffraction limit. Today's best storage rings and X-ray optics deliver sufficiently monochromatic beams with $\sim 10^{12}$ X-rays/s/$\mu$m$^2$. Beams of far higher specific intensity are possible with lower-emittance X-ray sources. For example, if suitable X-ray optics can be devised, an ERL design advocated by Cornell University would be able to deliver $\sim 10^{11}$–$10^{12}$ X-rays/s/nm$^2$ (14).

**Radiation damage.** The ability to extract structural information from protein crystals is ultimately limited by radiation damage, a broad term encompassing a multitude of destructive processes resulting from ionizing radiation (32, 80, 101). These processes include bond scission, chemical alteration, and charge movement, leading to displacement of atoms and consequent loss of inherent structure. In the noncryocooled case, chemically destructive entities, such as free radicals, readily diffuse and multiply damage. This takes significant time. As a result, the damage continues to increase even after the X-ray beam is turned off; i.e., radiation damage is time dependent and accumulates faster than linearly with the X-ray dose. (There are hints that at sufficiently high dose rates at storage ring sources, one might be able to begin to outrun radiation damage—this is a current area of research. This is not to be confused with dosing in femtoseconds at XFELs, where damage can be outrun.) If the crystal is cryocooled prior to irradiation to prevent diffusion, damage will be localized to primary sites of electron ejection and Compton scattering. In this case, the damage increases linearly with the X-ray dose (absorbed X-ray energy per unit mass of specimen). The damage is locked in at cryotemperatures by the inability of atoms to move about. If the crystal is warmed to allow diffusion, degraded diffraction from the irradiated regions quickly becomes evident.

Another consequence of the absorption of X-ray energy is the production of heat. At low rates of X-ray fluence the heat may be effectively conducted out of the crystal to surrounding cold gas in a cryostream. As the specific X-ray intensity rises, however, a point is reached where energy is deposited faster than it can be conducted away and the local temperature rises. This ultimately sets the limit of microbeam intensity for crystallography at storage ring sources.

XFELs can produce microbeams of $>10^{12}$ X-rays in a pulse only femtoseconds long. The pulse is scattered from a microcrystal before the tens of femtoseconds required for atomic nuclei to move appreciably. The result is that the diffracted X-rays have exited the sample before the sample is vaporized into plasma. This diffract-before-destroy regime gives XFELs the ability to largely outrun radiation damage. The number of diffracted X-rays, however, is ultimately limited by the number of electrons in the sample; after all, X-rays scatter primarily off the electrons. Typically 1 in 10 X-rays that interact with the sample is diffracted; the remainder photoeject electrons. At sufficiently high XFEL fluences, so many photoelectrons are ejected at the leading edge of the X-ray pulse that few electrons remain to scatter the remaining X-rays in the pulse. In other words, the diffraction becomes self-limiting (10, 39, 40, 112). Diffraction occurs only for the part of reciprocal space that intersects the Ewald sphere; thus, to gather a complete data set one must sample many orientations of crystals relative to the beam. The consequence is that, even with

XFELs, many microcrystals at different orientations need to be diffracted to obtain a complete data set. The primary potential advantage of XFELs is therefore the ability to obtain complete data sets with fewer unfrozen crystals than at storage rings or ERLs. Whether this translates in practice to a more feasible experiment depends on myriad details of experimental execution and facility access (see below).

**X-ray background reduction and efficient detectors.** X-ray background reduction is absolutely essential for microcrystallography. Holton & Frankel's (43) calculation that a complete data set can be obtained with a 1-μm crystal assumes recording of diffraction spots with a signal-to-noise (SNR) ratio of 2. In the absence of X-ray background and with an ideal detector, a SNR of 2 is achieved with $N = 4$ X-rays; i.e., SNR $= 4/\sqrt{4} = 2$. Few crystallographers would consider a measurement of four X-rays to be a viable diffraction spot, but this is simply because past experience typically involved detectors that had significant noise or sample situations with unnecessary X-ray background.

Modern electronic pixel array detectors, of both the photon-counting and photon-integrating variety, measure X-ray signals to an accuracy limited by the shot noise inherent in the signal being measured, i.e., the square root of the number of incident X-rays in the measurement area. In this regard, it is often said that modern pixel array detectors are noiseless. This phrase has no technical meaning, as no detector has infinitely precise ability to accurately measure X-ray signals. Limitations, which can be made small, arise from, e.g., variations in window absorption, partial transparency of the detector sensors to X-rays, and calibration imperfections. Another misconception is that photon-counting detectors make more accurate measurements than photon-integrating detectors do, especially for very-low-dose measurements. In fact, the accuracy with which a detector makes a measurement is dependent in all cases on the specific details of the detector and the measurement being made. For example, most photon-counting detectors installed on crystallographic beamlines to date lose X-rays because of charge division between neighboring pixels (35, 36). Newer technologies just now being developed promise to eliminate this flaw (8). Integrating detectors avoid this false-negative counting and perform in experiments even at remarkably low doses of a few X-rays per frame (6, 75), but these too are available only as custom devices. Even so, demonstrated technologies, for both photon-counting and photon-integrating pixel array detectors, prove that detectors need not be a limiting factor in SMX experiments.

Reducing background X-ray scatter to near-ideal levels is also possible but to date has not been implemented at practically any crystallographic beamlines. To set the scale, a suitable goal would be to reduce background scatter to levels inherent to the sample itself (see **Figure 1**). Most protein crystals are half water, the bulk of which is not crystallographically bound and therefore contributes to the diffuse background scatter. For a crystal 2 μm on a side, the irreducible scatter is therefore equivalent to 1 μm thickness of water. Water has roughly $10^3$ times the density of air or nitrogen; hence, background scatter equivalent to 1 μm water is obtained by an air or nitrogen main beam path length of 1 mm. If gas is required for cooling, helium, with roughly one-twentieth the scattering cross-section of air, is a better choice. SMX experiments at the LCLS occur in a vacuum, with background determined largely by the water or lipidic medium used to convey microcrystals into the XFEL beam (17, 60, 81, 102). This is necessary in part because X-ray windows would not survive passage of the XFEL beam.

X-ray windows and sample supports, when present, contribute X-ray background. Plastic windows usually have a scattering cross-section comparable to that of water, so two windows even 0.5 μm thick produce scatter equivalent to that of the internal crystal water. Likewise, crystals held, for example, in a 10-μm-thick film of vitreous water contribute many times the background scatter of the inherent crystal water.

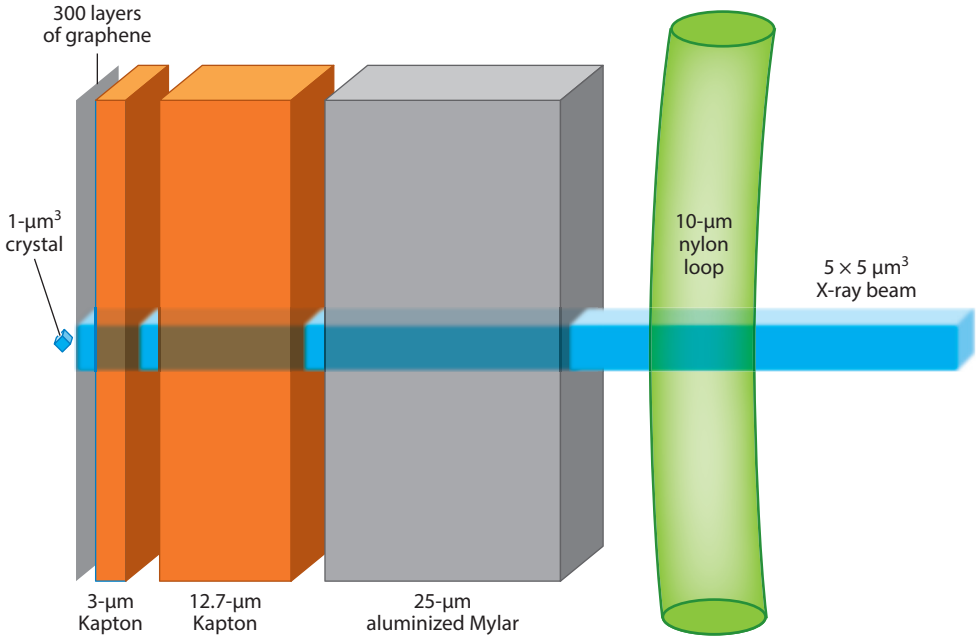


**Figure 1**

All stray matter in the 5 × 5 μm X-ray beam shown contributes to unwanted X-ray background. To appreciate relative magnitudes, consider a 1-μm³ protein crystal, shown at the left. It consists of about 50% water, which is the source of a minimum level of background scatter. All other materials that might be in the beam, some of which are shown to scale, contribute roughly in proportion to their volume in the beam. The desirability of eliminating all these sources of background is obvious. The graphene multilayer at the left represents 300 layers of graphene at the scale shown, because a few layers would be too thin a line to be seen in the drawing. The few layers of graphene that would actually be needed would contribute insignificantly to the X-ray background.

Ideally windows and sample supports should utilize materials that are no more than a few atoms thick for negligible background scatter. This is possible with graphene: A single layer of graphene, one carbon atom thick, is sufficiently strong to be used as a helium- and vacuum-tight window over multimicron-wide areas (19). Microcrystals encapsulated in liquid bubbles trapped between graphene sheets have been imaged in the high-vacuum environment of the electron microscope (109, 110). Wierman et al. (106) demonstrated the use of graphene sheets as a crystal support capable of spanning the better part of a millimeter. Free-standing, high-quality graphene is certain to become commercially available. Alternative window materials, such as silicon nitride windows hundreds of nanometers thick, are commercially available. Their thickness makes them less desirable than graphene but still sufficiently thin to serve for many SMX experiments.

**Crystal preparation and delivery into the X-ray beam.** SMX is justified by the assertion that large numbers of microcrystals of important systems are more readily obtainable than larger single crystals. Although the strength of the asserted case will become clearer as the community gathers experience, there is evidence that microcrystals are more easily obtained. Smaller crystals appear more readily in crystallization screens (79) of aqueously soluble proteins. Crystals produced by lipidic phase methods (49) are in most cases very small. Crystals grown in vivo in cells are necessarily

small (34, 81). Thus, even if the assertion is not universally true, it is likely to be true enough in certain important cases to warrant continued development of SMX.

A related question is whether the diffraction quality of microcrystals is generally better than that of larger crystals. Protein crystals usually have larger mosaicity than perfect crystals do, presumably because they consist of smaller mosaic blocks of more perfect crystals (68, 95). This suggests that as the size of the crystal approaches the size of the mosaic block, the mosaic spread should decrease. A reduction in disordered protein at the boundaries of mosaic blocks may also improve diffraction quality. Although there are few systematic studies on these issues, evidence for the improved quality of microcrystals is slowly accumulating as more microcrystal systems are studied. For example, Weierstall et al. (102) reported that they solved the structure of a G protein–coupled receptor complex with microcrystals using SMX at the LCLS. However, they were unsuccessful in solving the structure at a storage ring source with larger crystals because of poorer-quality diffraction from the larger crystals. Systematic investigations of the diffraction quality and, just as important, the heterogeneity in quality as a function of crystal size are needed. Typically, crystal mosaicity increases when crystals are cryocooled. It is not known how this effect scales with crystal size. It is possible that microcrystals are less disrupted by the cryocooling process. Systematic studies of questions such as these have been difficult to perform because microcrystals have been difficult to study. NGS are enabling in this regard. The studies should be done.

SMX depends on the availability of a sufficient quantity of suitable crystals and ways to serially feed these crystals into the beam. The literature to date on SMX at the LCLS is dominated by batch crystal preparation procedures (3, 17, 24, 48, 49, 53, 60, 81) and stochastic insertion of crystals into the beam with either an aqueous liquid jet (16, 96, 103) or a lipidic phase gel injector (102). The liquid injector is an ingenious device whereby a fluid jet studded with microcrystals is focused to micron sizes by a coaxial carrier gas sheath. Because the liquid stream moves at high speeds (meters per second), it consumes much protein. By contrast, the lipidic phase gel injector uses less protein because it slowly extrudes a few-microns-wide toothpaste-like column of highly viscous lipidic gel studded with membrane proteins within a coaxial gas sheath. Although the injector was designed to work with the lipidic gel phase in which membrane protein crystals are grown, it takes no stretch of imagination to consider using it with an appropriate polymer gel carrier for nonmembrane proteins.

The advantage of these methods is conceptual, if not actual, simplicity. But there is work to be done: Researchers must devise batch crystal preparation and delivery procedures to provide crystals of a homogenous size. Stochastic injection methods require decisions about the concentration of crystals to put into the carrier medium: If the concentration is too low, many laser pulses may encounter no crystals; at too high a concentration, more than one crystal at a time may be in the beam. Stochastic injection of crystals of heterogeneous sizes argues for a beam size that is larger than the average crystal size to maximize the probability of having a complete crystal in the beam. In this case, even if the crystal is centered in the beam, many X-rays bypass the crystal entirely, hitting only, perhaps, the carrier fluid and thereby contributing to unwanted background scatter. All these factors result in experiments that take both more time and more protein than ideally required. The consequence to date is that each SMX structure solved at the LCLS has required huge numbers of crystals. But these are early days for SMX at XFELs, and more efficient methods will certainly be devised.

It is instructive to compare two seminal SMX experiments, one done at the LCLS XFEL and one done at the PETRA III storage ring. Both experiments solved the structure of the glycosylated precursor complex of *Trypanosoma brucei* cathepsin B grown in vivo in bacteria. The LCLS structure solved at 2.1 Å used liquid jet injection involving many unfrozen crystals, of which $\sim 3 \times 10^5$ were diffracted (81). The PETRA III experiments used essentially the same source

of crystals—papers describing the two experiments have several authors in common—but in this case the crystals were spread across a ~20-μm-thick film of liquid spanning a 0.7-mm-diameter cryoloop, which was subsequently cryocooled. The loop was then raster-scanned using a microbeam and a conventional diffractometer at the microfocus P14 beamline at PETRA III. The loop yielded diffraction data from approximately 80 crystals that were used to solve the structure to 3.0 Å. The authors noted that background from the cryocooled liquid film was a limitation, but the background could have been be reduced if crystal supports derived from electron microscopy (68) or graphene (106) were used.

Obviously, one could consider doing a similar frozen cryoloop experiment at an XFEL that would be very conservative of protein. Cryocooled crystals, however, are biologically inactive. Alternatively, one might consider a spread of microcrystals at near room temperature, each within a tiny surrounding fluid volume, encapsulated between sheets of graphene. This is hardly fanciful—it has already been done with nanoparticles in electron microscope studies (109, 110).

Another very recent seminal SMX experiment at PETRA III used a flow of room-temperature lysozyme crystals down a glass capillary (98). A 9-μm-diameter beam was used with $2 \times 10^{12}$ 9,800-eV X-rays/s. The flow rate of crystals in the capillary resulted in exposures of 1 to 3 ms. Forty thousand diffraction patterns were acquired and refined at 2.1 Å resolution. Although the crystals were relatively large (~135 $\mu m^3$), this promising experiment supports our conclusion that SMX will become feasible at storage rings.

Ideally, all crystals would be produced at the beamline; all would be of a very similar size and fed one at a time into a microbeam with a cross-sectional diameter footprint that matched the projected area of the crystal. Scientists are currently developing microfluidic chips that screen proteins for crystallization conditions, make the crystals, and then shuttle them on-chip for serial in situ X-ray diffraction (41, 73, 91, 92). By controlling the feedback using small-growth volumes in the crystallization cells, scientists can create microdroplets with crystals of uniform size, with one crystal per microdrop (41). One can envision a system in which a microfluidic chip is used to create microcrystals of a uniform size that are then shuttled to an in situ diffraction chamber equipped with graphene or other ultrathin X-ray windows. Excess surrounding droplet fluid is then withdrawn, the crystal is diffracted while the entire chip undergoes small-angle oscillations, and then the crystal is flushed away. There is no reason why this cannot occur many times per second in an automated process. This would minimize handling of very delicate crystals.

**Data handling and diffraction signal strength.** One frontier experiment that motivated XFELs is the possibility of determining the structure of noncrystalline particles (11, 86, 96, 100). In this type of experiment many images are accumulated from individual particles encountering the X-ray pulse, one at a time. The challenge is to devise ways to sum the many images, given that each particle encounters the beam in a random, unknown orientation. Because the number of scattered X-rays is limited by the number of electrons in the particle, each diffraction image is severely Poisson noise limited, i.e., contains so few X-rays that no single image contains enough information to determine the orientation of the particle when it encountered the X-ray pulse. Such images are called sparse. Remarkably, so-called expand–maximize–compress (EMC) algorithms resolve this problem, given enough protein scattering events (27, 63). Practical demonstrations have proven that structures with even very sparse images can be recovered (6, 62, 74). Alternative methods to the EMC approach are also being developed (44), though it is not yet clear how well these approaches work with extremely sparse data.

As recently shown, EMC algorithms can be applied to sparse crystallographic data (5, 7). Further experiments needed to prove that EMC algorithms can be applied to SMX will likely soon be forthcoming. The key conclusion would be that it is not necessary for each microcrystal

to diffract enough X-rays to determine the orientation of the crystal. Given enough randomly oriented crystals, one can still determine the reciprocal space Bragg pattern, even though the orientation of each individual crystal is unknown. This conclusion has a remarkable corollary: The ability to do SMX is not limited by the strength of the X-ray source. In principle, SMX is possible with a conventional laboratory source, though the data collection times may be impractically long. Data collection times will certainly be feasible at storage ring sources.

SMX can generate copious quantities of data and is pushing X-ray crystallography into previously uncharted areas of truly massive data sets. Procedures that have been used to turn SMX into real structures are evolving quickly (9, 18, 25, 31, 85, 96, 104, 105).

## The Future of SMX

Given the considerations above, it is useful to speculate about the future of SMX as this serves to stimulate research. We confine attention to static SMX; the special case of very fast time-resolved SMX (70, 87) is beyond the scope of this review.

Compelling considerations that will shape the future of SMX include (*a*) the availability of SMX beamlines and better detectors, (*b*) a reduction in X-ray background, (*c*) a desire to reduce the amount of protein needed to obtain a complete data set, and (*d*) the size of the crystals. What kind of X-ray source will enable SMX? SMX is already being performed at XFELs and at bright storage rings (see below). The feasibility of SMX will certainly be enhanced as XFELs become more stable, perhaps with seeded operation; as ERLs and UESRs are built; and as technical innovations downstream of the source come online. The arguments given above therefore suggest that the capabilities of SMX will grow at all the different types of very bright sources. The simple availability of beamlines and the wealth of crystals in the micron-sized range will catalyze a rapid increase in storage-ring-based capabilities. Much depends on the size of the crystals. As crystal sizes shrink below 1 μm, XFEL sources will look increasingly attractive, at least initially. Further, one can envision high-throughput XFEL capabilities. But as crystal sizes shrink and technical advances allow researchers to manipulate crystals in high-vacuum environments, electron microscope diffraction will also become increasingly attractive (1, 58, 68, 69, 88, 90), given that electrons have $\sim 10^4$ times the scattering cross-section of X-rays and that difficulties resulting from multiple scattering decrease with sample thickness.

Storage ring beamlines can readily be adapted to deal with cryocooled crystals ranging from 1 to 20 μm (34). This size range is also readily within reach of room-temperature experiments (98). In cases in which sample protein is limited, in situ diffraction in microfluidic chips will become especially useful (41, 73).

Especially as crystals sizes shrink, background reduction will compel SMX beamlines to utilize vacuum environments from source to detector except for perhaps the immediate environment around the crystals. In the case of cryocooled crystals spread on, e.g., graphene or thin polymer films, the crystals themselves can be introduced into the vacuum environment. Because XFEL pulses are shorter in duration than heat transfer times, it would simply be necessary to maintain enough distance between crystals so that the sample destruction induced by a XFEL pulse is sufficiently isolated from the remaining crystals. Continuous cryocooling may be required for storage ring experiments in which exposure times are longer than phonon timescales. One can envision, for example, crystals on a planar graphene support that is raster-scanned through a microbeam in an enclosed space on the order of a millimeter across through which there is a flow of cold helium gas. This enclosed space is in the vacuum environment of the beamline, and X-rays are admitted into and out of the enclosed space via small windows made of graphene or other low-background scattering material.

The toothpaste extrusion–injection system (102) is an elegant room-temperature solution that uses relatively little protein. It is likely to be adapted for both XFEL and storage ring systems, and for both membrane and fully aqueous proteins. Noncryocooled crystals can suffer only very brief exposure to vacuum. A gas sheath was utilized in XFEL experiments; however, in a storage ring beamline it is easy to visualize use within a narrow enclosed space as described in the previous paragraph. Likewise, microfluidic chip delivery systems with integral vacuum windows are likely to be developed for storage ring SMX (41, 73). These systems may be more difficult to use at XFELs because the windows would likely be destroyed by the XFEL pulse.

In summary, these are exciting times for developments in SMX. XFELs have catalyzed innovative thinking, both for XFEL and non-XFEL SMX. One thing is certain: Future crystallography options will be far more diverse than they have been in the past.

## NONCRYSTALLINE SPECIMENS

The possibility of using XFELs to image single particles (e.g., proteins or viruses) in vacuum has been well reviewed elsewhere (11, 61, 62, 71, 86). It is not discussed here other than to note that the process is challenging and faces intense competition from single-particle imaging by electron microscopy (38). Rather, we discuss structural measurements of molecules in solution that are enabled by NGS.

### Time-Resolving Fast Structural Changes

Very-short-duration NGS X-ray pulses enable the study of very rapid structural changes. An elegant example is an experiment at the LCLS (4) that examined fast changes upon light absorption in the photosynthetic reaction center (PRC). The PRC faces unique problems of energy management because the energy of a single green light photon is approximately equal to the activation energy for unfolding the molecule. Photons absorbed by the light-harvesting antennae in the PRC are rapidly funneled to the reaction center through dedicated, specialized channels. Excess energy deposited in the protein is hypothesized to emanate as displacement waves before damage can be done by a process called protein quakes (2, 111).

Multiphoton absorption was used to trigger the PRC (22) and wide-angle X-ray scattering (WAXS) was monitored for progress of the structural change. Red light laser pulses 500 fs in duration were focused onto a microjet of PRC solution prior to the arrival of X-ray pulses. The delay time between the laser and XFEL pulses was calibrated to $\leq$5 ps, and WAXS patterns were collected over a series of 41 time delays up to 100 ps. Curves showing the difference in scattering between activated and dark (unactivated) molecules were generated at each time point. The light-induced perturbation appeared within a few picoseconds and subsequently decayed over $\sim$10 ps. Importantly, the perturbation preceded the propagation of heat through the protein.

The results relied on knowledge of the equilibrium molecular structure of the complex (23), as well as molecular dynamics simulations and modeling. A combination of molecular dynamics simulations of heat deposition and flow in a molecule and spectral decomposition of the time-resolved difference scattering curves provided the basis for an understanding of energy propagation in the system. Because the light pulse was tuned to the frequency of the photosystem antennae, cofactors were heated to few thousand Kelvins, which decayed with a halftime of $\sim$7 ps via heat flow to the remainder of the PRC. Signatures of protein structural changes appeared with clarity in oscillations of a component (termed C2) of the spectral decomposition of the data. This study illustrates both the rapid evolution of the technology and experimental prowess of the field and an application to a biologically important problem.

Another example of a study of a light-activated system measured changes in the size and shape of photoactive yellow protein (PyP) following photoactivation (21). This work was a sequel to an earlier study in which PyP was studied by time-resolved Laue crystallography (89). The Laue study illustrated a PyP photocycle involving four intermediate states. The solution scattering study was undertaken in part to dispel questions about the effects of lattice constraints on the observed structural changes in the protein.

The experimental protocol contained a number of innovative elements. The PyP solution was pumped with a circularly polarized laser flash. Because the flash is absorbed primarily by the *p*-coumaric acid chromophore, the protein molecules being excited are selected to align the chromophore transition dipole with the electric field of the illumination. This alignment gave rise to mildly anisotropic scattering, providing additional information in the pattern. Isolated ~100-ps X-ray pulses at the BioCARS 14-ID-B beamline at the US Department of Energy's Advanced Photon Source probed the PyP solution. High-resolution data ($q_{max} = 2.5$ Å$^{-1}$) were observed. The pulse length was longer than the lifetime of the excited state, such that there were multiple opportunities to excite each molecule. The story of how the authors handled the weak signal from the experiment is a lesson in care and thoughtfulness.

In this study, a rapid 0.3% compaction of the protein was modeled along the direction of the electronic transition moment of the *p*-coumaric acid, accompanied by expansion along perpendicular directions, producing a change in overall volume of approximately −0.25%. The 150-ps time resolution of the experiment was too slow to track the compaction, suggesting avenues for future work on XFELs. The solution scattering results were largely supportive of the original model derived from the Laue crystal work. These two studies illustrate requirements for future studies: a worthy photo-activatable system; X-ray pulses capable of producing WAXS in time intervals shorter than the time constants of the process being monitored; structural knowledge of the unactivated (dark) system; and an ability to use scattering to model the changes arising from the activation.

## Structure from Molecules in Solution

Traditional solution scattering involves X-ray illumination of a volume of the solution and collection of the resulting X-ray scatter. Because the sample contains many randomly oriented molecules, the measured diffraction pattern is cylindrically symmetric (i.e., azimuthally averaged) about the incident beam axis. The resulting curve of scattered intensity versus angle from the incident beam is relatively smooth. Even so, the resulting low-resolution curve, obtained from small-angle X-ray scattering (SAXS), can yield important information about the size, shape, and volume of the molecule (15, 37, 57, 76, 78). Work by Svergun & Koch (99) and Shneerson & Saldin (93) has resulted in a suite of computer programs that facilitate SAXS analysis.

The extraction of much information from a simple curve challenges intuition. However, Hura et al. (47) calculated SAXS curves for many proteins and showed that molecules of different folds do indeed have distinguishable curves. Also, because proteins are compact objects (i.e., have a finite support), the range of possible curves is severely limited.

Still, SAXS reconstructions without additional constraints can vary considerably. Fast, intense NGS pulses offer additional constraints: SAXS data can be obtained on timescales that are fast relative to the rotational motion of the particles. This sort of experiment has come to be called fluctuational solution scattering (FSS). Kam and colleagues (50–52) pointed out the possibilities of FSS long ago, but the requisite X-ray sources did not exist. Now XFELs are motivating intense interest in FSS (26, 28, 29, 56, 59, 77, 82, 83). The reader is referred to a masterful tutorial by Kirian (55) for insights into how FSS works.

FSS data methodology is in its formative stages. Liu et al. (59) applied angular correlation methods to simulated data from two globular proteins, the icosahedral *Satellite tobacco necrosis virus* (STNV) protein and the torus-shaped protein peroxiredoxin. Reconstructions were carried out at low resolution using an elaborated version of the Kam method, in which expanded Zernike polynomials and symmetrized basis functions played a key role. The spatial correlation coefficients between the reconstructed models and the original Protein Data Bank model were >75%. Intermediate results of the reconstruction yielded computed curves equivalent to those obtained in traditional SAXS experiments; reconstructions based solely on these models were flawed compared with reconstructions that received the full FSS treatment. Liu et al. (59) also examined an experimental system of ellipsoidal iron oxide nanoparticles and produced promising reconstructions.

An important feasibility experiment performed at the LCLS examined dumbbell-shaped particles formed from two polystyrene spheres of equal size that were dispersed in micron-sized aerosol droplets (97). Cylindrical symmetry of the specimen was used to recover the three-dimensional angular correlation function. Obtaining the corresponding calculations for an object with no symmetry would be a much more formidable task. Nevertheless, this paper appears to represent the first three-dimensional reconstruction of an object using FSS 2D data. As such, it serves as a pathway to more realistic specimens.

Another important proof-of-principle experiment for FSS involved ab initio structure determination of gold rods from soft X-ray diffraction patterns of arrays of such rods confined to a plane (82). The rods were approximately 90 $\times$ 25 nm and were imaged lying on a 30-nm-thick silicon nitride membrane. The authors formed the angular multiparticle correlation functions for each of the observed diffraction patterns and summed these to derive the single-particle correlation function from which the low-resolution structure of the rods was determined.

The Kam formalism is not limited to low-resolution reconstructions, as shown by another recent proof-of-principle experiment on silver nanocrystals (65). Because the SSRL (Stanford Synchrotron Radiation Lightsource) storage ring used as a source has relatively long pulses, the silver nanocrystal suspension was frozen to preclude particle rotation. Three angular correlation functions were computed: within the ring containing the 111 reflections; within the ring containing the 200 reflections; and between the rings, obtaining the 111 and the 200 reflections. The resultant correlation signals at effectively atomic resolution were in agreement with theory. Conventional powder analysis techniques applied to the same specimens would have produced only two signals, those from the 111 ring and the 200 ring. Coherent X-ray imaging, including the angular correlation peaks, provided five signals. One can foresee many important applications of this technique as methodology improves. This study opens the door to high-resolution studies in more complex systems, such as proteins.

In conclusion, to illustrate future potential, we consider a specific biological system, RNA folding, that might benefit from the capacity of NGS to map out large new regions of this experimental space. The world of noncoding RNAs is filled with large structures essential for protein synthesis, splicing, and many other cellular processes (107, 108). The folding and assembly of these systems is of intense interest. RNA folding differs in many ways from protein folding. The unfolded state is generally characterized by persistent secondary structure, that is, the existence of RNA helices, hairpins, and related secondary structures. Formation of tertiary structure normally requires increasing concentrations of divalent cations, particularly magnesium, as well as the presence of companion proteins in many cases. Folding is also characterized by the existence of stable intermediates that exist at $Mg^{2+}$ concentrations below that necessary for complete folding. In addition, complex kinetics leads to the formation of off-pathway structures. Finally, the range of time constants involved is very broad.

Imagine the experimental problem of mapping the folding of a complicated RNA or ribonucleoprotein complex. We want to know the time constants for the formation and dissipation of kinetic intermediates, as well as their structures. We would like to know the structures and concentrations of intermediates at local minima in the folding process. Much more detailed questions will arise for each individual system.

Although solution SAXS has already made significant contributions to our understanding of RNA folding (76), NGS time-resolved WAXS and SAXS provide new opportunities. One great benefit of RNA as a system for study is that partial structures of many of the intermediates will be known. The ability to recover the intensity transform from SAXS, or to bin structural information in the case of alternative confirmations, depends critically on relatively modest amounts of additional information. For example, Elser (28) has shown that recovery of intensity transform from solution scattering experiments on particles having no symmetry and fully random orientations is undetermined. When the orientation of one axis in the particle is fixed in space, the problem becomes tractable. Thus, the variety of known structures in the RNA system becomes an enormous advantage. In addition, the high phosphate content provides stronger scattering, improving signal-to-noise ratios. What would be needed are X-ray pulses short enough to freeze the rotations of the particles and outrun overt radiation damage. NGS will provide such pulses.

## CONCLUSION

NGS are contributing to biostructural science both by providing new capabilities and by inspiring new approaches at existing storage ring sources. The resultant excitement is palpable. The ultimate benefits to biology are certain to be immense.

### SUMMARY POINTS

1. SMX refers to crystallographic methods used to determine the structure of macromolecules from a series of small crystals (a few microns across or smaller) that are individually too small to yield complete data sets prior to irreversible radiation damage.
2. SMX will be most useful for systems in which only small crystals are readily obtained. Examples of particular interest include membrane proteins and macromolecular complexes.
3. As the technology advances, it is increasingly clear that SMX will be feasible both at next-generation X-ray sources (X-ray free-electron lasers, energy recovery linac sources, and ultra-low-emittance storage rings) and existing high-spectral-brightness storage ring sources.
4. Intense X-ray free-electron laser pulses enable powerful new methods, such as WAXS from noncrystalline specimens and solutions, for femtosecond studies.

### FUTURE ISSUES

1. A great deal of developmental work remains to be done before SMX becomes routine at any synchrotron source. Currently (as of December 2014), SMX for unfrozen crystals micron-sized or smaller has been successfully demonstrated only at X-ray free-electron lasers.

2. Single-particle imaging at XFELs awaits significant progress in source intensity, noise reduction, detector technology, and other experimental aspects.
3. Femtosecond time-resolved X-ray studies of biological specimens are still at the very early stages. One may anticipate rapid progress at X-ray free-electron laser sources as user time becomes increasingly available.

## DISCLOSURE STATEMENT

The authors are not aware of any affiliations, memberships, funding, or financial holdings that might be perceived as affecting the objectivity of this review.

## ACKNOWLEDGMENTS

S.M.G. is grateful for support from CHESS (supported by NSF and NIH-NIGMS via DMR-1332208), MacCHESS (NIH GM-103485), and DOE (DE-FG02-10ER46693). E.E.L. is grateful for support from the NSF (DBI-1231306).

## LITERATURE CITED

1. Amunts A, Brown A, Bai XC, Llácer JL, Hussain T, et al. 2014. Structure of the yeast mitochondrial large ribosomal subunit. *Science* 343:1485–89
2. Ansari A, Berendzen J, Bowne SF, Frauenfelder H, Iben IET, et al. 1985. Protein states and proteinquakes. *PNAS* 82:5000–4
3. Aquila A, Hunter MS, Doak RB, Kirian RA, Fromme P, et al. 2012. Time-resolved protein nanocrystallography using an X-ray free-electron laser. *Opt. Express* 20:2706–16
4. Arnlund D, Johansson LC, Wickstrand C, Barty A, Williams GJ, et al. 2014. Visualizing a protein quake with time-resolved X-ray scattering at a free-electron laser. *Nat. Methods* 11:923–26
5. Ayyer K. 2014. *Reconstructing images from sparse data*. PhD Thesis, Cornell Univ. Press
6. Ayyer K, Philipp HT, Tate MW, Elser V, Gruner SM. 2014. Real-space X-ray tomographic reconstruction of randomly oriented objects with sparse data frames. *Opt. Express* 22:2403–13
7. Ayyer K, Philipp HT, Tate MW, Wierman JL, Elser V, Gruner SM. 2014. Determination of crystallographic intensities from sparse data. *IUCrJ* 2:29–34
8. Ballabriga R, Alozy J, Campbell M, Fiederle M, Fröjdh E, et al. 2013. The Medipix3RX: a high resolution, zero dead-time pixel detector readout chip allowing spectroscopic imaging. *J. Instrum.* 8:2
9. Barends TRM, Foucar L, Botha S, Doak RB, Shoeman RL, et al. 2014. De novo protein crystal structure determination from X-ray free-electron laser data. *Nature* 505:244–47
10. Barty A, Caleman C, Aquila A, Timneanu N, Lomb L, et al. 2012. Self-terminating diffraction gates femtosecond X-ray nanocrystallography measurements. *Nat. Photonics* 6:35–40
11. Barty A, Küpper J, Chapman HN. 2013. Molecular imaging using X-ray free-electron lasers. *Annu. Rev. Phys. Chem.* 64:415–35
12. Bass M, ed. 2001. *Handbook of Optics*. *Volume III: Classical Optics*, *Vision Optics*, *X-Ray Optics*. New York: McGraw-Hill
13. Bei M, Borland M, Cai Y, Elleaume P, Gerig R, et al. 2010. The potential of an ultimate storage ring for future light sources. *Nuclear Instrum. Methods Phys. Res. A* 622:518–35
14. Bilderback DH, Brock JD, Dale DS, Finkelstein KD, Pfeifer MA, Gruner SM. 2010. Energy recovery linac (ERL) coherent hard X-ray sources. *New J. Phys.* 12:035011
15. Blanchet CE, Svergun DI. 2013. Small-angle X-ray scattering on biological macromolecules and nanocomposites in solution. *Annu. Rev. Phys. Chem.* 64:37–54

16. Bogan MJ. 2013. X-ray free electron lasers motivate bioanalytical characterization of protein nanocrystals: serial femtosecond crystallography. *Anal. Chem.* 85:3464–71
17. Boutet S, Lomb L, Williams GJ, Barends TRM, Aquila A, et al. 2012. High-resolution protein structure determination by serial femtosecond crystallography. *Science* 337:362–64
18. Brehm W, Diederichs K. 2014. Breaking the indexing ambiguity in serial crystallography. *Acta Crystallogr. D* 70:101–9
19. Bunch JS, Verbridge SS, Alden JS, van der Zande AM, Parpia JM, et al. 2008. Impermeable atomic membranes from graphene sheets. *Nano Lett.* 8:2458–62
20. Chapman HN, Fromme P, Barty A, White TA, Kirian RA, et al. 2011. Femtosecond X-ray protein nanocrystallography. *Nature* 470:73–77
21. Cho HS, Schotte F, Dashdorj N, Kyndt J, Anfinrud PA. 2013. Probing anisotropic structure changes in proteins with picosecond time-resolved small-angle X-ray scattering. *J. Phys. Chem. B* 117:15825–32
22. Cogdell RJ, Gall A, Köhler J. 2006. The architecture and function of the light-harvesting apparatus of purple bacteria: from single molecules to in vivo membranes. *Q. Rev. Biophys.* 39:227–324
23. Deisenhofer J, Epp O, Sinning I, Michel H. 1995. Crystallographic refinement at 2.3 Å resolution and refined model of the photosynthetic reaction centre from *Rhodopseudomonas viridis*. *J. Mol. Biol.* 246:429–57
24. Demirci H, Sierra RG, Laksmono H, Shoeman RL, Botha S, et al. 2013. Serial femtosecond X-ray diffraction of 30S ribosomal subunit microcrystals in liquid suspension at ambient temperature using an X-ray free-electron laser. *Acta Crystallogr. F* 69:1066–69
25. Donatelli JJ, Sethian JA. 2014. Algorithmic framework for X-ray nanocrystallographic reconstruction in the presence of the indexing ambiguity. *PNAS* 111:593–98
26. Elser V. 2003. Phase retrieval by iterated projections. *J. Opt. Soc. Am. A* 20:40–55
27. Elser V. 2009. Noise limits on reconstructing diffraction signals from random tomographs. *IEEE Trans. Inf. Theory* 55:4715–22
28. Elser V. 2011. Strategies for processing diffraction data from randomly oriented particles. *Ultramicroscopy* 111:788–92
29. Elser V. 2011. Three-dimensional structure from intensity correlations. *New J. Phys.* 13:123014
30. Falcone R, Jacobsen C, Kirz J, Marchesini S, Shapiro D, Spence J. 2011. New directions in X-ray microscopy. *Contemp. Phys.* 52:293–318
31. Foucar L, Barty A, Coppola N, Hartmann R, Holl P, et al. 2012. CASS—CFEL-ASG software suite. *Comput. Phys. Commun.* 183:2207–13
32. Garman EF, Nave C. 2009. Radiation damage in protein crystals examined under various conditions by different methods. *J. Synchrotron Radiat.* 16:129–32
33. Gasbarro A, Bazarov I. 2014. Reduced forms of the Wigner distribution function for the numerical analysis of rotationally symmetric synchrotron radiation. *J. Synchrotron Radiat.* 21:289–99
34. Gati C, Bourenkov G, Klinge M, Rehders D, Stellato F, et al. 2014. Serial crystallography on in vivo grown microcrystals using synchrotron radiation. *IUCrJ* 1:87–94
35. Gimenez EN, Ballabriga R, Campbell M, Horswell I, Dolbnya I, et al. 2011. Characterization of Medipix3 with synchrotron radiation. *IEEE Trans. Nuclear Sci.* 58:323–32
36. Gimenez EN, Ballabriga R, Campbell M, Horswell I, Llopart X, et al. 2011. Study of charge-sharing in MEDIPIX3 using a micro-focused synchrotron beam. *J. Instrum.* 6:C01031
37. Glatter O, Kratky O. 1982. *Small Angle X-Ray Scattering*. New York: Academic
38. Greber BJ, Boehringer D, Leitner A, Bieri P, Voigts-Hoffmann F, et al. 2014. Architecture of the large subunit of the mammalian mitochondrial ribosome. *Nature* 505:515–19
39. Hau-Riege SP. 2012. Photoelectron dynamics in X-ray free-electron-laser diffractive imaging of biological samples. *Phys. Rev. Lett.* 108:238101
40. Hau-Riege SP. 2013. Nonequilibrium electron dynamics in materials driven by high-intensity X-ray pulses. *Phys. Rev. E* 87:053102
41. Heymann M, Opthalage A, Wierman JL, Akella S, Szebenyi DME, et al. 2014. Room-temperature serial crystallography using a kinetically optimized microfluidic device for protein crystallization and on-chip X-ray diffraction. *IUCrJ* 1:349–60

42. Holton JM. 2009. A beginner's guide to radiation damage. *J. Synchrotron Radiat.* 16:133–42
43. Holton JM, Frankel KA. 2010. The minimum crystal size needed for a complete diffraction data set. *Acta Crystallogr. D* 66:393–408
44. Hosseinizadeh A, Schwander P, Dashti A, Fung R, D'Souza RM, Ourmazd A. 2014. High-resolution structure of viruses from random diffraction snapshots. *Philos. Trans. R. Soc. B* 369:20130326
45. Howells MR, Beetz T, Chapman HN, Cui C, Holton JM, et al. 2009. An assessment of the resolution limitation due to radiation-damage in X-ray diffraction microscopy. *J. Electron Spectrosc. Relat. Phenom.* 170:4–12
46. Hunter MS, Fromme P. 2011. Toward structure determination using membrane-protein nanocrystals and microcrystals. *Methods* 55:387–404
47. Hura GL, Menon AL, Hammel M, Rambo RP, Poole FL 2nd, et al. 2009. Robust, high-throughput solution structural analyses by small angle X-ray scattering (SAXS). *Nat. Methods* 6:606–12
48. Johansson LC, Arnlund D, Katona G, White TA, Barty A, et al. 2013. Structure of a photosynthetic reaction centre determined by serial femtosecond crystallography. *Nat. Commun.* 4:2911
49. Johansson LC, Arnlund D, White TA, Katona G, DePonte DP, et al. 2012. Lipidic phase membrane protein serial femtosecond crystallography. *Nat. Methods* 9:263–65
50. Kam Z. 1977. Determination of macromolecular structure in solution by spatial correlation of scattering fluctuations. *Macromolecules* 10:927–34
51. Kam Z, Gafni I. 1985. Three-dimensional reconstruction of the shape of human wart virus using spatial correlations. *Ultramicroscopy* 17:251–62
52. Kam Z, Koch MHJ, Bordas J. 1981. Fluctuation X-ray-scattering from biological particles in frozen solution by using synchrotron radiation. *PNAS* 78:3559–62
53. Kang HJ, Lee C, Drew D. 2013. Breaking the barriers in membrane protein crystallography. *Int. J. Biochem. Cell Biol.* 45:636–44
54. Kim KJ. 1986. Brightness, coherence and propagation characteristics of synchrotron radiation. *Nuclear Instrum. Methods Phys. Res. A* 246:71–76
55. Kirian RA. 2012. Structure determination through correlated fluctuations in X-ray scattering. *J. Phys. B* 45:223001
56. Kirian RA, Schmidt KE, Wang X, Doak RB, Spence JC. 2011. Signal, noise, and resolution in correlated fluctuations from snapshot small-angle X-ray scattering. *Phys. Rev. E* 84:011921
57. Koch MHJ, Vachette P, Svergun DI. 2003. Small-angle scattering: a view on the properties, structures and structural changes of biological macromolecules in solution. *Q. Rev. Biophys.* 36:147–227
58. Kuhlbrandt W. 2014. The resolution revolution. *Science* 343:1443–44
59. Liu HG, Poon BK, Saldin DK, Spence JCH, Zwart PH. 2013. Three-dimensional single-particle imaging using angular correlations from X-ray laser data. *Acta Crystallogr. A* 69:365–73
60. Liu W, Wacker D, Gati C, Han GW, James D, et al. 2013. Serial femtosecond crystallography of G protein-coupled receptors. *Science* 342:1521–24
61. Loh ND. 2014. A minimal view of single-particle imaging with X-ray lasers. *Philos. Trans. R. Soc. B* 369:20130328
62. Loh ND, Bogan MJ, Elser V, Barty A, Boutet S, et al. 2010. Cryptotomography: reconstructing 3D Fourier intensities from randomly oriented single-shot diffraction patterns. *Phys. Rev. Lett.* 104:225501
63. Loh NTD, Elser V. 2009. Reconstruction algorithm for single-particle diffraction imaging experiments. *Phys. Rev. E* 80:026705
64. McNeil BWJ, Thompson NR. 2010. X-ray free-electron lasers. *Nat. Photonics* 4:814–21
65. Mendez D, Lane TJ, Sung J, Sellberg J, Levard C, et al. 2014. Observation of correlated X-ray scattering at atomic resolution. *Philos. Trans. R. Soc. B* 369:20130315
66. Nave C, Garman EF. 2005. Towards an understanding of radiation damage in cryocooled macromolecular crystals. *J. Synchrotron Radiat.* 12:257–60
67. Nave C, Hill MA. 2005. Will reduced radiation damage occur with very small crystals? *J. Synchrotron Radiat.* 12:299–303
68. Nederlof I, Li YW, van Heel M, Abrahams JP. 2013. Imaging protein three-dimensional nanocrystals with cryo-EM. *Acta Crystallogr. D* 69:852–59

69. Nederlof I, van Genderen E, Li YW, Abrahams JP. 2013. A Medipix quantum area detector allows rotation electron diffraction data collection from submicrometre three-dimensional protein crystals. *Acta Crystallogr. D* 69:1223–30
70. Neutze R, Moffat K. 2012. Time-resolved structural studies at synchrotrons and X-ray free electron lasers: opportunities and challenges. *Curr. Opin. Struct. Biol.* 22:651–59
71. Neutze R, Wouts R, van der Spoel D, Weckert E, Hajdu J. 2000. Potential for biomolecular imaging with femtosecond X-ray pulses. *Nature* 406:752–57
72. Ohashi H, Yamazaki H, Yumoto H, Koyama T, Senba Y, et al. 2013. Stable delivery of nano-beams for advanced nano-scale analyses. *J. Phys.* 425:052018
73. Perry SL, Guha S, Pawate AS, Bhaskarla A, Agarwal V, et al. 2013. A microfluidic approach for protein structure determination at room temperature via on-chip anomalous diffraction. *Lab Chip* 13:3183–87
74. Philipp HT, Ayyer K, Tate MW, Elser V, Gruner SM. 2012. Solving structure with sparse, randomly-oriented X-ray data. *Opt. Express* 20:13129–37
75. Philipp HT, Ayyer K, Tate MW, Elser V, Gruner SM. 2013. Recovering structure from many low-information 2-D images of randomly selected samples. *J. Phys.* 425:192016
76. Pollack L. 2011. SAXS studies of ion–nucleic acid interactions. *Annu. Rev. Biophys.* 40:225–42
77. Poon HC, Saldin DK. 2011. Beyond the crystallization paradigm: structure determination from diffraction patterns from ensembles of randomly oriented particles. *Ultramicroscopy* 111:798–806
78. Putnam CD, Hammel M, Hura GL, Tainer JA. 2007. X-ray solution scattering (SAXS) combined with crystallography and computation: defining accurate macromolecular structures, conformations and assemblies in solution. *Q. Rev. Biophys.* 40:191–285
79. Quevillon-Cheruel S, Dominique L, Leulliot N, Graille M, Poupon A, et al. 2004. The Paris-Sud yeast structural genomics pilot-project: from structure to function. *Biochimie* 86:617–23
80. Ravelli RBG, Garman EF. 2006. Radiation damage in macromolecular cryocrystallography. *Curr. Opin. Struct. Biol.* 16:624–29
81. Redecke L, Nass K, DePonte DP, White TA, Rehders D, et al. 2013. Natively inhibited *Trypanosoma brucei* cathepsin B structure determined by using an X-ray laser. *Science* 339:227–30
82. Saldin DK, Poon HC, Bogan MJ, Marchesini S, Shapiro DA, et al. 2011. New light on disordered ensembles: ab initio structure determination of one particle from scattering fluctuations of many copies. *Phys. Rev. Lett.* 106:115501
83. Saldin DK, Poon HC, Schwander P, Uddin M, Schmidt M. 2011. Reconstructing an icosahedral virus from single-particle diffraction experiments. *Opt. Express* 19:17318–35
84. Sanishvili R, Yoder DW, Pothineni SB, Rosenbaum G, Xu SL, et al. 2011. Radiation damage in protein crystals is reduced with a micron-sized X-ray beam. *PNAS* 108:6127–32
85. Sauter NK, Hattne J, Grosse-Kunstleve RW, Echols N. 2013. New Python-based methods for data processing. *Acta Crystallogr. D* 69:1274–82
86. Schlichting I, Miao J. 2012. Emerging opportunities in structural biology with X-ray free-electron lasers. *Curr. Opin. Struct. Biol.* 22:613–26
87. Schmidt M. 2013. Mix and inject: reaction initiation by diffusion for time-resolved macromolecular crystallography. *Adv. Condens. Matter Phys.* **http://dx.doi.org/10.1155/2013/167276**
88. Schmidt-Krey I, Cheng Y, eds. 2013. *Electron Crystallography of Soluble and Membrane Proteins.* Heidelberg, Ger.: Springer
89. Schotte F, Cho HS, Kaila VRI, Kamikubo H, Dashdorj N, et al. 2012. Watching a signaling protein function in real time via 100-ps time-resolved Laue crystallography. *PNAS* 109:19256–61
90. Shi D, Nannenga BL, Iadanza MG, Gonen T. 2013. Three-dimensional electron crystallography of protein microcrystals. *Elife* 2:e0 1345:1–17
91. Shim JU, Cristobal G, Link DR, Thorsen T, Fraden S. 2007. Using microfluidics to decouple nucleation and growth of protein crystals. *Crystal Growth Design* 7:2192–94
92. Shim JU, Cristobal G, Link DR, Thorsen T, Jia YW, et al. 2007. Control and measurement of the phase behavior of aqueous solutions using microfluidics. *J. Am. Chem. Soc.* 129:8825–35
93. Shneerson VL, Saldin DK. 2009. Molecular shapes from small-angle X-ray scattering: extension of the theory to higher scattering angles. *Acta Crystallogr. A* 65:128–34

94. Sliz P, Harrison SC, Rosenbaum G. 2003. How does radiation damage in protein crystals depend on X-ray dose? *Structure* 11:13–19
95. Snell EH, Helliwell JR. 2005. Macromolecular crystallization in microgravity. *Rep. Prog. Phys.* 68:799–853
96. Spence JCH, Weierstall U, Chapman HN. 2012. X-ray lasers for structural and dynamic biology. *Rep. Prog. Phys.* 75:102601
97. Starodub D, Aquila A, Bajt S, Barthelmess M, Barty A, et al. 2012. Single-particle structure determination by correlations of snapshot X-ray diffraction patterns. *Nat. Commun.* 3:1276
98. Stellato F, Oberthür D, Liang M, Bean R, Gati C, et al. 2014. Room-temperature macromolecular serial crystallography using synchrotron radiation. *IUCrJ* 1:204–12
99. Svergun DI, Koch MHJ. 2002. Advances in structure analysis using small-angle scattering in solution. *Curr. Opin. Struct. Biol.* 12:654–60
100. Thibault P, Elser V. 2010. X-ray diffraction microscopy. *Annu. Rev. Condens. Matter Phys.* 1:237–55
101. Warkentin M, Badeau R, Hopkins J, Thorne RE. 2011. Dark progression reveals slow timescales for radiation damage between T = 180 and 240 K. *Acta Crystallogr. D* 67:792–803
102. Weierstall U, James D, Wang C, White TA, Wang D, et al. 2014. Lipidic cubic phase injector facilitates membrane protein serial femtosecond crystallography. *Nat. Commun.* 5:3309
103. Weierstall U, Spence JCH, Doak RB. 2012. Injector for scattering measurements on fully solvated biospecies. *Rev. Sci. Instrum.* 83:035108
104. White TA, Barty A, Stellato F, Holton JM, Kirian RA, et al. 2013. Crystallographic data processing for free-electron laser sources. *Acta Crystallogr. D* 69:1231–40
105. White TA, Kirian RA, Martin AV, Aquila A, Nass K, et al. 2012. CrystFEL: a software suite for snapshot serial crystallography. *J. Appl. Crystallogr.* 45:335–41
106. Wierman JL, Alden JS, Kim CU, McEuen PL, Gruner SM. 2013. Graphene as a protein crystal mounting material to reduce background scatter. *J. Appl. Crystallogr.* 46:1501–7
107. Woodson SA. 2010. Compact intermediates in RNA folding. *Annu. Rev. Biophys.* 39:61–77
108. Woodson SA. 2011. RNA folding pathways and the self-assembly of ribosomes. *Acc. Chem. Res.* 44:1312–19
109. Yuk JM, Kim K, Aleman B, Regan W, Ryu JH, et al. 2011. Graphene veils and sandwiches. *Nano Lett.* 11:3290–94
110. Yuk JM, Park J, Ercius P, Kim K, Hellebusch DJ, et al. 2012. High-resolution EM of colloidal nanocrystal growth using graphene liquid cells. *Science* 336:61–64
111. Zang C, Stevens JA, Link JJ, Guo LJ, Wang LJ, Zhong DP. 2009. Ultrafast proteinquake dynamics in cytochrome *c*. *J. Am. Chem. Soc.* 131:2846–52
112. Ziaja B, Chapman HN, Faustlin R, Hau-Riege S, Jurek Z, et al. 2012. Limitations of coherent diffractive imaging of single objects due to their damage by intense X-ray radiation. *New J. Phys.* 14:114015